Towards seismic moment tensor inversion for source mechanism

Faranak Mahmoudian and Kristopher A. Innanen

ABSTRACT

The objective of this work is to obtain seismic moment tensor, M_{pq}, from amplitude inversion of multi-component microseismic data. M_{pq} describes source mechanism and can be decomposed into double-couple, isotropic and compensated-linear-vector-dipole (related to tensile fracturing) components - the tensile components might show a correlation to hydrocarbon production rate. The retrieved M_{pq} are sensitive to the accuracy of the source location, the accuracy of the velocity model, and the receiver array geometry. Excluding the first two factors, the determination of the proper observation geometry for which the full moment tensor is resolvable was sought. Having two vertical or surface receiver arrays, or a combination of them, M_{pq} may be fully determined using the inversion of P- and S-wave first arrival amplitudes. This configuration, which is sufficient for this purpose, includes the receiver arrays located in the vertical and horizontal part of a single deviated well. To avoid the cumbersome task of picking first-arrival amplitudes, we considered a waveform inversion scheme based on the method proposed by Vavryčuk and Kühn (2012). This method combines inversions in both the time and frequency domains. The first requirement was the inversion for the source-time function in the frequency domain. Second, a time domain inversion for M_{pq} using the source-time function calculated in the first step was initiated. For this waveform inversion, we have not yet achieved an accurate retrieval of M_{pq}, but we have been able to obtain an accurate source-time function estimate.

INTRODUCTION

Determination of the seismic moment tensor is a routine procedure in earthquake seismology (e.g., Dziewonski et al., 1981; Šílený, 1998; Shearer, 1999). The seismic moment tensor provides a general representation of the seismic source and can be determined from inversion of seismic amplitudes detected on surface/downhole receiver arrays. M_{pq} is commonly decomposed into a double couple tensor, produced by shear faulting, and a non-double couple tensor, produced by the opening or closing of faults (tensile faulting) (Vavryčuk, 2001) (see Appendix A). Hence M_{pq} provides information related to the physical processes at the source (e.g., Ross et al., 1999; Maxwell and Urbancic, 2001; Foulger et al., 2004; Vavryčuk, 2007).

Moment tensor inversions are less frequently performed on microseismic events for the purpose of extracting source mechanism. Figure 1 displays a cartoon of microseismic clouds for a hypothetical well. It is commonly assumed that a higher production is associated with a denser microseismic cloud. However for this hypothetical well, good production comes from the side-track with the less dense microseismic cloud. If the source mechanism of such microseismic events were analyzed, there would be some possibility of correlating the production rate with the higher percentage of tensile fracturing from the decomposition of the M_{pq}. With this motivation, this research is aimed at obtaining an accurate source parameters using the moment tensor inversion as a long-term goal.

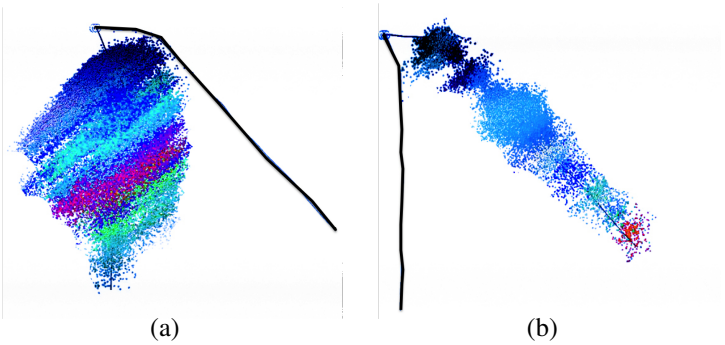

(a) (b)

FIG. 1: A hypotetical well with two side-tracks and known production rate. (a) Left side-track with denser microseismic clouds and a low production rate. (b) Right side-track with less dense microseismic clouds and a high production rate. This cartoon of microseismic events are produced based on the first author's experience with unconventinal shale reservoirs in central Alberta. This plot although fictional, displays a case often observed in production of shale reservoirs going through hydraulic fracturing enhansement.

A point source with a general radiation pattern can be represented by the seismic moment tensor. The complete moment tensor is characterized by the six independent elements of the 3×3 symmetric moment tensor matrix. The 3-components of the displacement wavefield observed at the geophone located at $\vec{x}$ are expressed as (Aki and Richards, 2002, equation 3.23)

$$u_n(\vec{x}, t) = m_{pq}(t) * g_{np,q}(\vec{x}, t), \tag{1}$$

where $*$ is convolution symbol, summation convention is applied, and $n = (1, 2, 3)$. $m_{pq}(t)$, the time-dependent seismic moment tensor, describes the properties of the source. $g_{np,q}(\vec{x}, t)$,* the spatial derivative of the Green's function, describes the properties of the medium. For a point source, the time-dependent moment tensor can be factorized as

$$m_{pq}(t) = M_{pq} S(t), \tag{2}$$

where M_{pq} is the seismic moment tensor that we are trying to invert for, and $S(t)$ is the source-time function. Determination of M_{pq} is a demanding procedure influenced by several factors. The most important of these are::

1. Observations from many stations (good station coverage of the focal zone), to extract all the six M_{pq}, which will be termed the receiver geometry effect.
2. Deriving the representative source-time function.
3. An accurate knowledge of the velocity model and focal location, in order to calculate the Green's functions.
4. The availability of quality data, to enable event picking in the source location step.

*The Green's functions are due to a point source at $\vec{x_s}$. The precise notation is $g(\vec{x}, \vec{x_s}, t)$ which the source term has been dropped out for simplicity.

In microseismic monitoring the effect of receiver's geometry in determination of M_{pq} is a known issue, point (1) listed above. The complete moment tensor can be determined from noise-free amplitudes of P- and S-waves from the event observed at three stations at least, with the condition that the raypaths must have different directions and must not lie in a single plane (Vavryčuk, 2007). This means that using data from a single borehole or surface array, the full seismic moment tensor is not resolvable. The impossibility of recovering the complete moment tensor from a single borehole has been established by Nolen-Hoeksema and Ruff (2001). Vavryčuk (2007) used the far-field approximation of the P- and S-wave Green's function in homogenous isotropic and anisotropic media to show that a single-azimuth data set recorded in one vertical well can not resolve the dipole perpendicular to the plane of geophones and the hypocenter. He showed analytically and using numerical modelling experiments that for receivers on a single borehole (a) inverting only P-waves amplitudes the three components of the moment tensor (M_{11}, M_{33}, M_{13}) can be retrieved, (b) when inverting S-waves, the M_{12}, M_{13}, M_{23} and the difference $M_{11} - M_{33}$ are retrievable, (c) inverting P- and S-wave data simultaneously yields five components of the moment tensor, M_{22} is not recoverable. He also demonstrated that using two borehole arrays in two different wells (observing the source from two different azimuths), the full M_{pq} is retrievable using P- and S-wave amplitudes simultaneously. Rodriguez et al. (2011) examined the resolvability of the full moment tensor under single-well monitoring geometry and demonstrated that only five of the six M_{pq} can be correctly estimated when the observation plane is aligned with two axes of the moment tensor reference system. They also suggested that using receiver array in a deviated well satisfies the required receivers' orientation for a full moment tensor inversion.

We report the effect of receiver geometry on retrieval of the seismic moment tensor, for vertical or surface arrays while ignoring the other three factors listed above. We found that the full moment tensor may be determined using P- and S-wave amplitude data from two receiver arrays (vertical or surface) observing the source from two distinctive azimuths, regardless of being aligned with the source reference system or not. Using data from a single vertical or surface array, five M_{pq} may be resolved, however only if the observation plane is aligned with the source reference system. Having receivers in both vertical and horizontal part of a deviated well, we found, regardless of the azimuth of the well, the full moment tensor is resolvable when using P- and S-wave amplitude data.

Another key factor in recovering seismic moment tensor is the determination of the time variation of the source, point (2) listed above. The source-time function is often assumed to have a simple form, a single pulse appearing in all elements of the moment tensor (equation 2). While this is an oversimplified assumption for earthquake sources, due to the possibility of having a complex fault geometry, equation 2 is a reasonable assumption for a point source directly applicable to microseismic events. With this assumption, the determination of M_{pq} and the source-time function is still a non-linear problem (equations 1-2) and requires non-linear inversions of the seismic waveform (Šílený, 1998). Avoiding non-linear inversions, a number of studies used P/S amplitude ratios (e.g., Julian and Foulger, 1996; Rau et al., 1996; Hardebeck and Shearer, 2003) or absolute P- and S amplitudes (e.g., Ebel and Bonjer, 1990; Nakamura et al., 1999) to determine the source mechanism. Vasco (1989) estimated the source-time function through the singular value decomposition (SVD) of three-component (3C) displacement data in the frequency domain; The eigenvector associ-

ated with the largest singular value coincides with the most dominant source-time function. He showed the adequacy of assuming a single source-time function with the application of this SVD technique on a nuclear explosion data. Vavryčuk and Kühn (2012) presented a two step linear waveform inversion applied in time and frequency domain to estimate the source-time function and the M_{pq}. First, they performed a frequency domain inversion for the single source-time function (similar to Vasco (1989) method). Second, a time-domain inversion for the M_{pq} was performed using the source-time function calculated in the first step. In this report, we followed Vavryčuk and Kühn (2012) two-step linear inversion to estimate the source-time function and M_{pq} using the seismic waveform. Testing this method on numerical model data generated with TIGER software, we obtained the source-time function that was a good match to the initial wavelet used in the modelling.

This report presents a general view of moment tensor theory, describes the linear inversion of P- and S-wave first-arrival amplitudes for the seismic moment tensor to examine the resolvability of the seismic moment tensor under single/multiple vertical/surface receiver array configuration, and the two-step waveform inversion, yet linear, for the source-time function and the seismic moment tensor.

GENERAL VIEW OF SEISMIC MOMENT TENSOR

Definition

In a Cartesian coordinate system (x_1, x_2, x_3), the seismic moment tensor is a 3×3 symmetric matrix of force couples M_{pq} (e.g., Shearer, 1999; Lay and Wallace, 1995; Madariaga, 2007) as

$$M = \begin{bmatrix} M_{11} & M_{12} & M_{13} \\ M_{21} & M_{22} & M_{23} \\ M_{31} & M_{32} & M_{33} \end{bmatrix}. \tag{3}$$

A **force couple** M_{pq} is defined as a pair of opposing forces pointing in the p direction, separated in the q direction (Figure 8 8(a)). For angular momentum of a system to be preserved, for every M_{pq} there must exists a complementary equal couple M_{qp} that balances the forces ($M_{pq} = M_{qp}$) (Shearer, 1999). Thus, the seismic moment tensor is a symmetric matrix with six independent elements $(M_{11}, M_{22}, M_{33}, M_{23}, M_{13}, M_{12})$.

Radiation pattern from moment tensor sources

For a homogenous isotropic medium, from equation 1, the *n*'th component of the **far-field** displacement wavefield observed at point $\vec{x}$, from a point source at $\vec{x_s}$, can be written as the sum of the far-field P- and S-wave displacements, $u_n(\vec{x}, t) = u_n^P(\vec{x}, t) + u_n^S(\vec{x}, t)$. The far-field P- and S-wave displacements are expressed as (Aki and Richards, 2002, third term in equation 4.29)

$$u_n^P(\vec{x}, t) = \frac{\gamma_n \gamma_p \gamma_q}{4\pi\rho\alpha^3 r} M_{pq} \dot{S}\left(t - \frac{r}{\alpha}\right), \tag{4}$$

$$u_n^S(\vec{x}, t) = \frac{(\delta_{np} - \gamma_n \gamma_p)\gamma_q}{4\pi\rho\beta^3 r} M_{pq} \dot{S}\left(t - \frac{r}{\beta}\right), \tag{5}$$

where ρ is the density, α is the P-wave velocity, β is the S-wave velocity, and $r = |\vec{r}| = |\vec{x} - \vec{x_s}|$ is source-receiver distance. Recall that the summation convention is used for the repeated indexes (p and q). The blue coloured terms, are called radiation patterns $\mathscr{F}^P(\vec{x})$ and $\mathscr{F}^S(\vec{x})$ for P-wave and S-wave respectively, where γ_n are the direction cosines for the source-receiver vector, $\vec{r}$, so that $\gamma_n = \frac{(\vec{x}-\vec{x_s})_n}{r}$. Dropping out the M_{pq} in the radiation patterns, will define the Green's function that we started with in equation 1. Hence for a homogenous isotropic medium, the spatial derivatives of the P- and S-wave Green's function are

$$g^P_{np,q}(\vec{x}) = \frac{\gamma_n\gamma_p\gamma_q}{4\pi\rho\alpha^3 r}, \tag{6}$$

$$g^S_{np,q}(\vec{x}) = \frac{(\delta_{np} - \gamma_n\gamma_p)\gamma_q}{4\pi\rho\beta^3 r}. \tag{7}$$

P-waves from a moment tensor point source have a typical dipolar radiation patterns, while S-waves have torodial (doughnut-shaped) radiation patterns (Madariaga, 2007). Figure 2 displays P- and S-wave radiation pattern, as well as the radiation pattern of SV- and SH-waves, for a few moment tensor sources. See Appendix B for more explanation on how these radiation patterns have been coded. Note, the SV- and SH-waves do not exist for an isotropic homogeneous layer and its only upon propagation on layering media that SV- and SH-waves come to exist. Nevertheless, as wave propagation in a homogeneous medium has been used to understand and analyze the wave propagation in more complicated media, the SV- and SH radiation patterns are also presented in Figure 2.

MOMENT TENSOR INVERSION

Moment tensor inversions use seismic radiation patterns to calculate the M_{pq} and therefore seismic source mechanism. There are three main techniques for moment tensor inversion, a) first-arrival polarity methods, b) amplitude methods, and c) full-waveform methods. Eyre and van der Baan (2015) presents a good overview of the basic and fundamentals of these techniques for microseismic application. We use an amplitude technique to investigate the effect of receiver's geometry on the resolvability of the moment tensor and a simple full-waveform technique to first extract source-time function and then the moment tensor, while not examining the first-arrival polarity technique.

Regardless of which moment tensor inversion technique is used, results of the inversion will be more reliable if sensor locations allow for a good sampling of the focal sphere (e.g., Eaton and Forouhideh, 2011; Rodriguez et al., 2011; Eyre and van der Baan, 2015). While numerous sensors are available in earthquake application making the full moment tensor solvable by having enough sampling of the wavefield, restrictions in microseismic acquisition geometry is a considerate challenge for the applications of moment tensor inversions. The most common practice configuration in microseismic monitoring is the single-well approach which all the receivers observe the microseismic event from a single azimuth view. Next we examine the resolvability of the full moment tensor for data acquired during microseismic monitoring surveys using both single and multiple vertical/surface receiver arrays. We present a proper resolvability analyses assessing if using a given acquisition geometry the full moment tensor can be accurately retrieved from an inversion.

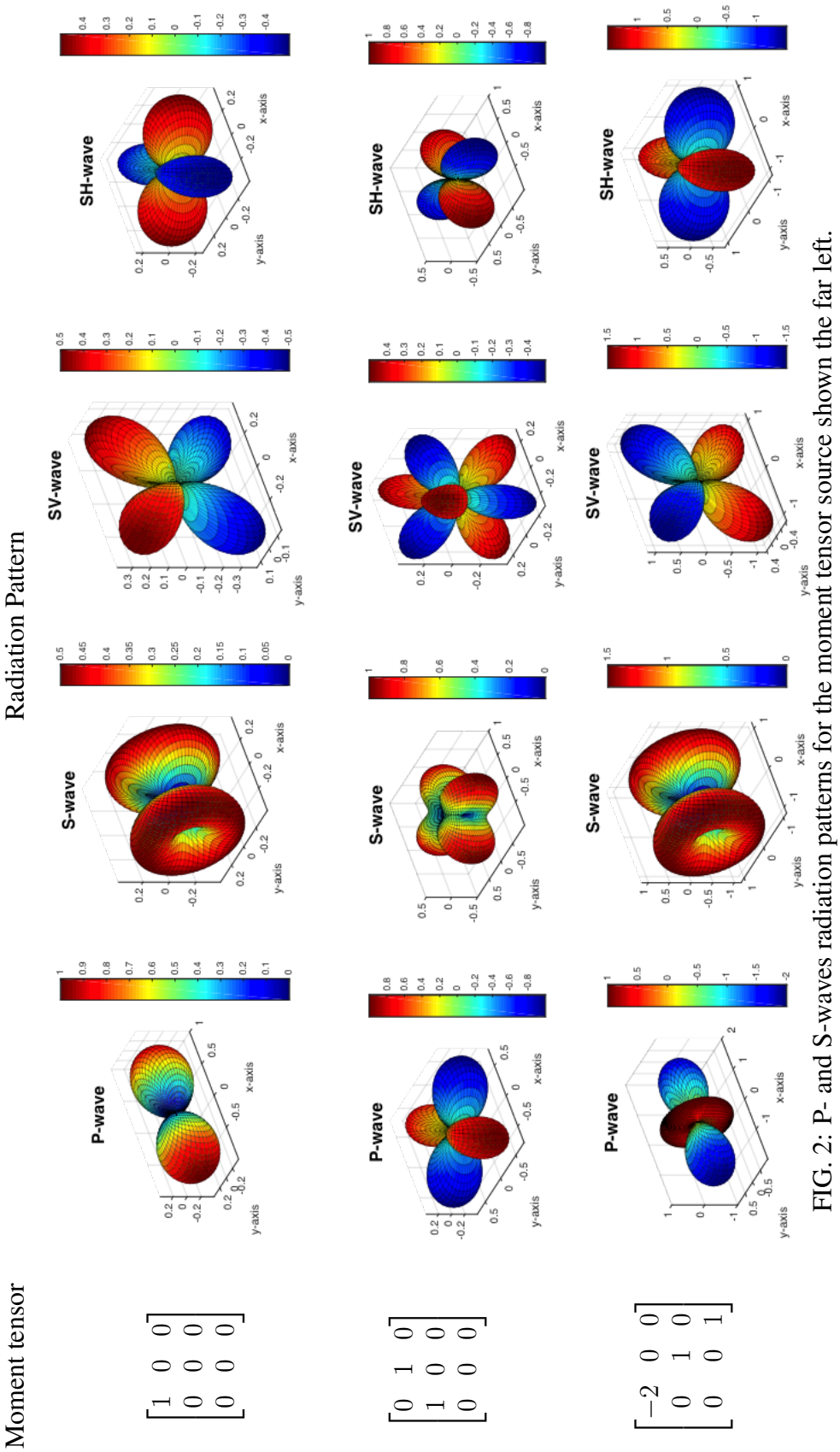

FIG. 2: P- and S-waves radiation patterns for the moment tensor source shown the far left.

RECEIVER GEOMETRY EFFECT

Our resolvability analysis is based on the linear relation between radiated P- and S-wave amplitudes and the M_{pq} elements (equations 4 and 5). The 3C P- and S-wave far-field displacement amplitudes, can be used to construct a linear system of equations, to solve for full moment tensor, as (see Appendix B for the derivation)

$$\begin{pmatrix} u_{p1}^{(1)} \\ u_{p2}^{(1)} \\ u_{p3}^{(1)} \\ \vdots \\ u_{p1}^{(N)} \\ u_{p2}^{(N)} \\ u_{p3}^{(N)} \\ u_{s1}^{(1)} \\ u_{s2}^{(1)} \\ u_{s3}^{(1)} \\ \vdots \\ u_{s1}^{(N)} \\ u_{s2}^{(N)} \\ u_{s3}^{(N)} \end{pmatrix} = AB \begin{pmatrix} (1) & \gamma_1^3 & \gamma_1\gamma_2^2 & \gamma_1\gamma_3^3 & 2\gamma_1\gamma_2\gamma_3 & 2\gamma_1^2\gamma_3 & 2\gamma_1^2\gamma_2 \\ & \gamma_2\gamma_1^2 & \gamma_2^3 & \gamma_2\gamma_3^2 & 2\gamma_2^2\gamma_3 & 2\gamma_2\gamma_1\gamma_3 & 2\gamma_2^2\gamma_1 \\ & \gamma_3\gamma_1^2 & \gamma_3\gamma_2^2 & \gamma_3^3 & 2\gamma_3^2\gamma_2 & 2\gamma_3^2\gamma_1 & 2\gamma_3\gamma_1\gamma_2 \\ & \vdots & \vdots & \vdots & \vdots & \vdots & \vdots \\ (N) & \gamma_1^3 & \gamma_1\gamma_2^2 & \gamma_1\gamma_3^3 & 2\gamma_1\gamma_2\gamma_3 & 2\gamma_1^2\gamma_3 & 2\gamma_1^2\gamma_2 \\ & \gamma_2\gamma_1^2 & \gamma_2^3 & \gamma_2\gamma_3^2 & 2\gamma_2^2\gamma_3 & 2\gamma_2\gamma_1\gamma_3 & 2\gamma_2^2\gamma_1 \\ & \gamma_3\gamma_1^2 & \gamma_3\gamma_2^2 & \gamma_3^3 & 2\gamma_3^2\gamma_2 & 2\gamma_3^2\gamma_1 & 2\gamma_3\gamma_1\gamma_2 \\ (1) & \gamma_1-\gamma_1^3 & -\gamma_1\gamma_2^2 & -\gamma_1\gamma_3^2 & -2\gamma_1\gamma_2\gamma_3 & \gamma_3-2\gamma_1^2\gamma_3 & \gamma_2-2\gamma_1^2\gamma_2 \\ & -\gamma_2\gamma_1^2 & \gamma_2-\gamma_2^3 & -\gamma_2\gamma_3^2 & \gamma_3-2\gamma_2^2\gamma_3 & -2\gamma_2\gamma_1\gamma_3 & \gamma_1-2\gamma_2^2\gamma_1 \\ & -\gamma_3\gamma_1^2 & -\gamma_3\gamma_2^2 & \gamma_3-\gamma_3^3 & \gamma_2-2\gamma_3^2\gamma_2 & \gamma_1-2\gamma_3^2\gamma_1 & -2\gamma_3\gamma_1\gamma_2 \\ & \vdots & \vdots & \vdots & \vdots & \vdots & \vdots \\ (N) & \gamma_1-\gamma_1^3 & -\gamma_1\gamma_2^2 & -\gamma_1\gamma_3^2 & -2\gamma_1\gamma_2\gamma_3 & \gamma_3-2\gamma_1^2\gamma_3 & \gamma_2-2\gamma_1^2\gamma_2 \\ & -\gamma_2\gamma_1^2 & \gamma_2-\gamma_2^3 & -\gamma_2\gamma_3^2 & \gamma_3-2\gamma_2^2\gamma_3 & -2\gamma_2\gamma_1\gamma_3 & \gamma_1-2\gamma_2^2\gamma_1 \\ & -\gamma_3\gamma_1^2 & -\gamma_3\gamma_2^2 & \gamma_3-\gamma_3^3 & \gamma_2-2\gamma_3^2\gamma_2 & \gamma_1-2\gamma_3^2\gamma_1 & -2\gamma_3\gamma_1\gamma_2 \end{pmatrix}_{6N\times 6} \begin{pmatrix} M_{11} \\ M_{22} \\ M_{33} \\ M_{23} \\ M_{13} \\ M_{12} \end{pmatrix}_{6\times 1}, \tag{8}$$

where the superscripts are associated with receivers number (1) to (N), blue and red colours indicate P- and S-wave data respectively, and $AB = (A^{(1)} \quad A^{(1)} \quad A^{(1)} \quad \dots \quad A^{(N)} \quad A^{(N)} \quad A^{(N)} \quad B^{(1)} \quad B^{(1)} \quad B^{(1)} \quad \dots \quad B^{(N)} \quad B^{(N)} \quad B^{(N)})$. Equation 8 can be written in the simple form of

$$D = \underline{\mathbb{G}}M, \tag{9}$$

where D is data vector consist of the observed P- and S-wave amplitudes, the first two picks after the first arrivals, (in the fashion of data vector in equation 8), $\underline{\mathbb{G}}$ is called the geometry matrix, and $M = (M_{11}, M_{22}, M_{33}, M_{23}, M_{13}, M_{12})^T$ is the vector of model parameters to be inverted for. We solved equation 9 using a damped least-squares method, which the damping factor is decided based on the ratio of the maximum to minimum singular value of the geometry matrix ($\underline{\mathbb{G}}$).

Synthetics microseismic data

We tested the moment tensor inversion on 3C synthetics seismograms for a homogeneous isotropic medium with P-velocity $\alpha = 3000$ m/s, S-velocity $\beta = 2000$ m/s , and density $\rho = 2000$ Kg/m^3. We generated our synthetics in two ways, (1) (**modelled data 1**) convolving a source-time function with the P- and S-wave radiation patterns (equations 4 and 5), (2) (**modelled data 2**) using a 3D anisotropic elastic finite-difference modelling software called TIGER. TIGER is capable of producing 3C synthetics data for arbitrary acquisition geometry and employing a general source moment tensor. Appendix discusses the accuracy of synthetics data generated by TIGER when a general moment tensor source is used. Examining the receiver geometry effect, we used **modelled data 1**.

Inversion results

We generated 3C synthetics data recorded at multiple borehole/surface arrays and used the data in the moment tensor inversion described above. For all of our tests, a point source with the source moment tensor of

$$\begin{bmatrix} 1 & 6 & 0.5 \\ 6 & -2 & -1 \\ 0.5 & -1 & 4 \end{bmatrix}, \tag{10}$$

has been used. We examined the resolvability of the full moment tensor under single and multiple vertical/surface receiver array geometries. Figure 3 shows the the receiver array configuration, the estimated M_{pq}, the resolution matrix, and the singular values of the geometry matrix ($\underline{\mathbb{G}}$ in equation 9), using P-wave data only and simultaneous P- and S-wave data.

We analyze the resolvability of the inverse problem by using a model resolution matrix (e.g., Rodriguez et al., 2011; Mahmoudian et al., 2015). The product $R = \underline{\mathbb{G}^T\mathbb{G}}$ is defined as model resolution matrix (Menke, 1985). The resolution matrix becomes identity matrix when all the model components are linearly independent and accurately determined. For example, the existence of non-zero off-diagonal components ($R_{ij} \neq 0$) implies a linear correlation between model parameters m_i and m_j. Therefore, the resolution matrix provides important information on the resolvability of the model elements.

The Figure 3 shows the moment tensor inversion, for a single vertical borehole array, a single surface array, two vertical receiver arrays, and two surface arrays, in which the array of receivers is resided within a principal plane containing the source point. By a principal plane, we mean that the plane contains two axes of the reference coordinate system centred at the source. Employing only P-wave amplitudes in the moment tensor inversion, Figure 3 (middle column) shows that **(a)** Having a single vertical or surface array, only (M_{11}, M_{33}, M_{13}) elements will be resolved and there exists three null singular values (Figure 3 a-b). **(b)** Having two vertical or surface array, the $(M_{11}, M_{22}, M_{33}, M_{23}, M_{13}, M_{12})$ elements will be resolved and only M_{12} is unresolvable. There exists only one zero singular value (Figure 3 c-d). **(c)** The resolvability of the model parameters is insensitive to the distance between the array of receivers and the source. Employing P- and S-wave amplitudes simultaneously in the moment tensor inversion, Figure 3 (right column) shows that **(a)** Having a single vertical or surface array, all elements but the M_{22} will be resolved and there exists only one null singular values (Figure 3 a-b). **(b)** Having two vertical or surface array, the full moment tensor will be resolved (Figure 3 c-d). **(c)** The resolvability of the model parameters is insensitive to the distance between the array of receivers and the source.

Next, we present the moment tensor inversion results when the observation plane is not aligned with two axes of the source reference system. The Figure 4 shows the moment tensor inversion, for a single vertical borehole array, a single surface array, two vertical arrays, and two surface arrays which the receivers' array is placed outside the source principal planes. This will construct a reality receiver configuration, as we never know about the source reference system in advance. Employing only P-wave amplitudes in the moment

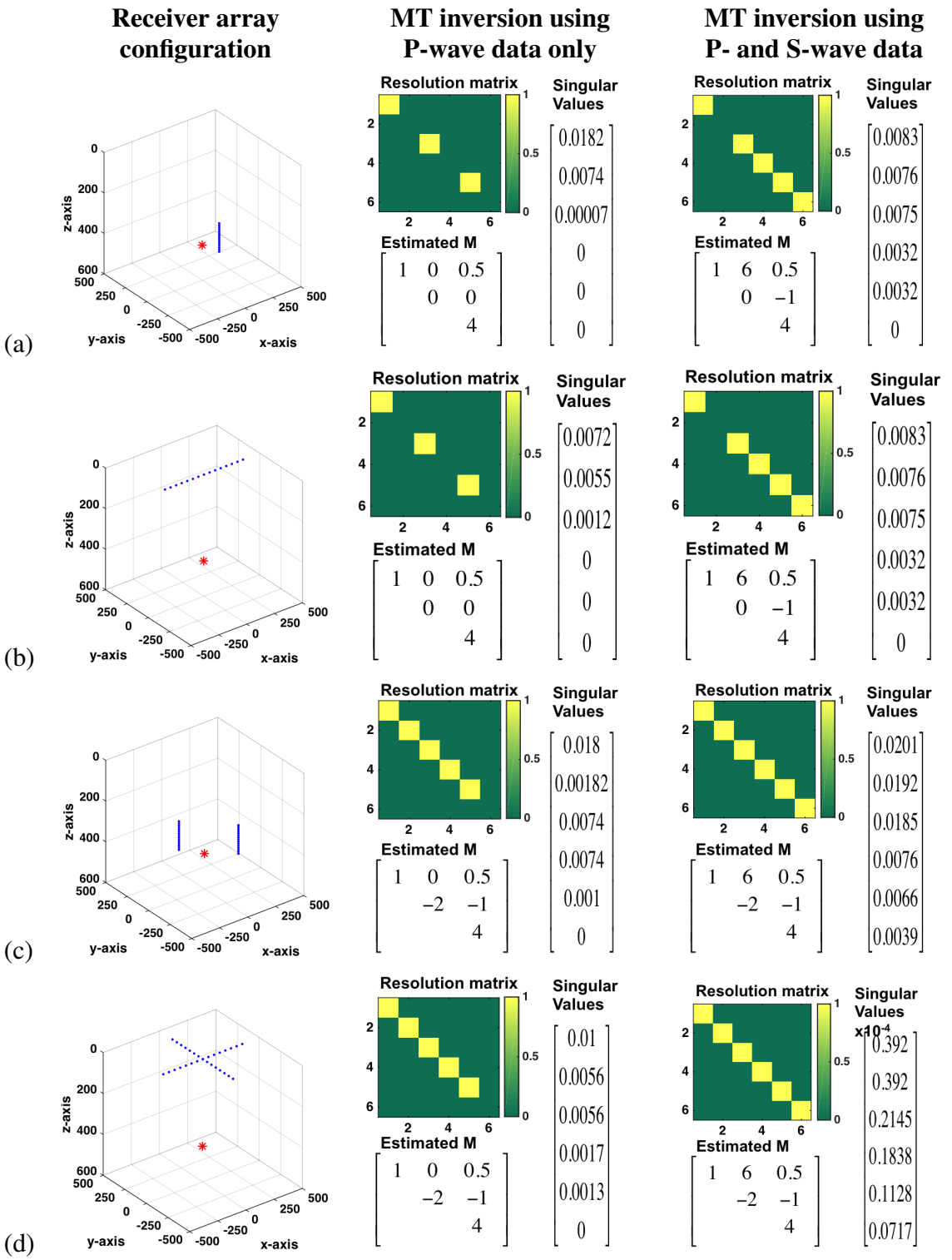

FIG. 3: Moment tensor inversion when the two axes of the source reference system constrained to the observation plane (a) A single borehole array. (b) A single surface array. (c) Two borehole receiver arrays. (d) Two surface receiver arrays. Left column is the receiver configuration, middle column is the moment inversion results using P-wave data only, and right column shows the moment tensor inversion results using P- and S-wave data simultaneously. In the inversion results for each case, the resolution matrix (its rows and columns are related to $(M_{11}, M_{22}, M_{33}, M_{23}, M_{13}, M_{12})$ respectively, the estimated moment tensor, and the singular values.

tensor inversion, Figure 4 (middle column) shows that **(a)** Having a single or two vertical arrays, none of elements but the M_{33} will be resolved, although there still exists three and one null singular values (Figure 4 a-b) respectively, which is similar to the above example that receivers located in the principal planes. This indicates that the resolution matrix is a better quantity to investigate the resolvability problem rather than the singular values or the condition number [†]. **(b)** Having a single surface array, none of elements will be resolved, although there still exists three null singular values (Figure 4 a-b). **(c)** Having two vertical or surface array, only M_{33} will be resolved, although there exists only one zero singular value (Figure 4 c-d). **(d)** The resolvability of the model parameters is insensitive to the distance between the array of receivers and the source. For the receivers' array outside the principal planes, employing P- and S-wave amplitudes simultaneously in the moment tensor inversion, Figure 3 (right column) shows that **(a)** Having a single vertical or surface array, non of the moment tensor elements will be resolved although there exists only one null singular values (Figure 3 a-b). **(b)** Having two vertical or surface array, the full moment tensor will be resolved (Figure 3 c-d). This is consistent with results of the two arrays located on the principal planes above.

Using only P-wave amplitudes for the full moment tensor to be resolved, three different receiver arrays are required (Vavryčuk, 2007). Figure 5 shows the moment tensor inversion results for arbitrary three vertical/surface arrays. The arrays do not require to be aligned with the source reference system and they could be completely arbitrary, as long as they constitute three different azimuths. Also, the inversion results are insensitive to the distance between the source and receiver arrays, similar to the results presented earlier. It is clear that the three receiver arrays configuration will resolve the full moment tensor when using P- and S-wave amplitude simultaneously as well.

In this section using numerical experiments we tried to show the theoretically predicted results in Vavryčuk (2007) for resolvability of the moment tensor using moment tensor inversion of multi borehole data. Also, our results are consistent with the results presented in Rodriguez et al. (2011) which they also showed using numerical experiments investigating single vertical well monitoring geometries. Rodriguez et al. (2011) investigated the full moment tensor resolvability by examining the resolution matrix for different combinations of source-receivers horizontal distance and azimuths of the borehole receiver array. Eaton and Forouhideh (2011) examined the resolvability of the moment tensor and demonstrated that the solid angle subtended by the receiver array, as viewed from the source location, plays a fundamental role. Our results for the sufficiency of two vertical/surface arrays in resolving the full moment tensor is just confirming Eaton and Forouhideh (2011) solid angle requirement.

As most of the microseismic monitoring are based on a single well configuration, we suggest to use receiver arrays in a deviated well which receivers are laid out in both vertical and nearly horizontal part of the well. This monitoring configuration would be similar to the two receiver arrays configuration above. Hence a simultaneous amplitude inversion, using data from a deviated well should satisfy the resolvability of full moment tensor. This

[†]Condition number is the ratio of the max-to-min singular values

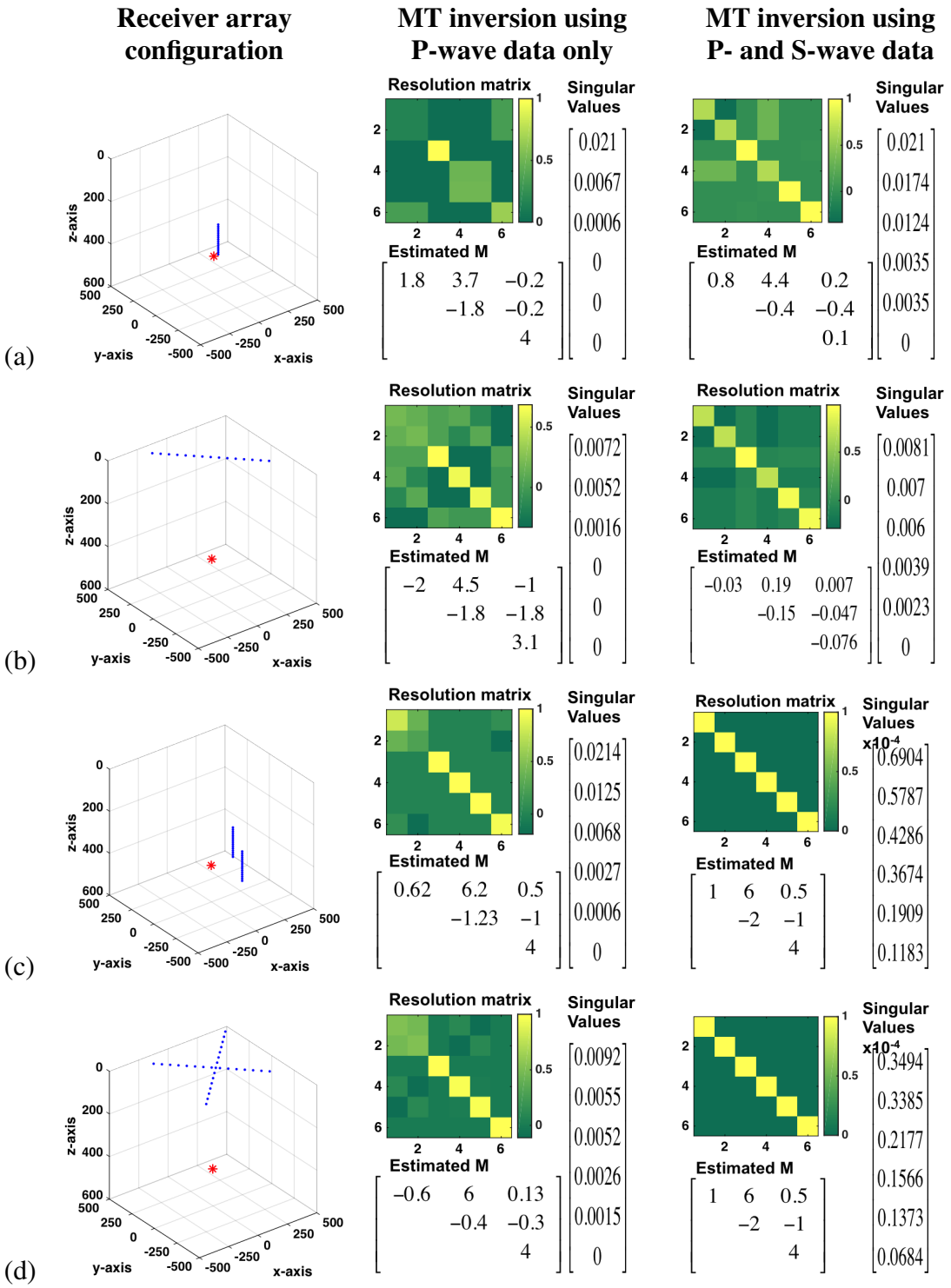

FIG. 4: Moment tensor inversion when the two axes of the source reference system are not constrained to the observation plane, with the same description as of Figure 3.

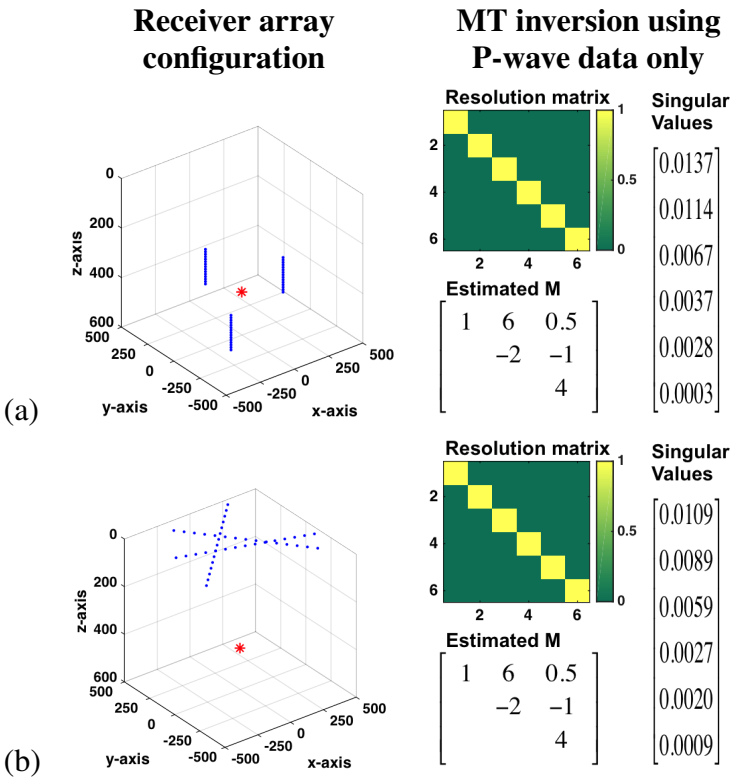

FIG. 5: Moment tensor inversion results when having three arbitrary (a) vertical or (b) surface receiver arrays, with the same description as of Figure 3.

deviated well configuration was suggested by Rodriguez et al. (2011). Figure 4 shows a deviated well, with receivers in both vertical and horizontal part of the well, that all six moment tensor elements are retrievable.

In this report the efficiency of the moment tensor inversion is tested on noise-free numerically generated data. In near future, we shall investigate the stability and robustness of the inversion by repeating the inversion on synthetics data contaminated by random noise. Also for this report, we assumed accurate microseismic source location and an accurate velocity model to single out the receiver geometry configuration in the resolvability of the moment tensor. Presented above, the amplitude data were picked from synthetics noise-free seismograms, we ignored all the complexity in picking the P- and S-wave first arrivals. For real data, first arrival amplitude picking is a cumbersome task and normally performed on data after being rotated into radial and transverse components. Additionally, knowing the source-time function that was used in generating the numerical modelled data, we applied the accurate scalar to remove the effect of source-time function. However, knowledge of the source-time function is never achieved in real data prior to the moment tensor inversion. Next following Vavryčuk and Kühn (2012), we apply a waveform inversion to first estimate the source-time function and second estimate the full moment tensor in a time-frequency approach. No amplitude picking is required for a waveform inversion.

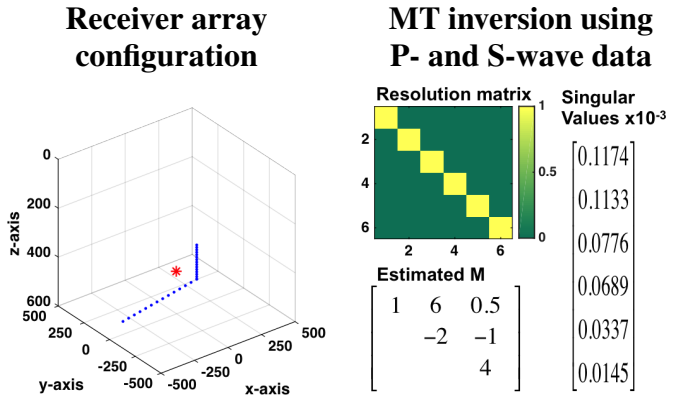

FIG. 6: Moment tensor inversion for a deviated well configuration.

MOMENT TENSOR INVERSION OF WAVEFORMS

Vavryčuk and Kühn (2012) presented a waveform inversion and yet linear for computing time-dependent moment tensors. Their method is performed in two steps and combines inversions in time and frequency domains. First, the inversion for the source-time function is performed in the frequency domain. Second, the time-domain inversion for moment tensor is performed using the source-time function calculated in the first step.

Step 1: Frequency-domain waveform inversion for source-time function

The displacement wavefield in frequency domain, taking Fourier transform of equation 1, transforms to

$$u_n(\vec{x},\omega) = m_{pq}(w) g_{np,q}(\vec{x},\omega). \tag{11}$$

Defining the functions $G_{ij}(\omega)(i=(1,2,3), j=(1,2,3,4,5,6))$, each Fourier transformed of the function G_{ij} in Appendix B, equation 11 can be expressed as a linear system of equations:

$$\begin{bmatrix} u_1^{(1)}(w) \\ u_2^{(1)}(w) \\ u_3^{(1)}(w) \\ \vdots \\ u_1^{(N)}(w) \\ u_2^{(N)}(w) \\ u_3^{(N)}(w) \end{bmatrix} = \begin{bmatrix} G_{11}^{(1)}(\omega) & G_{12}^{(1)}(\omega) & G_{13}^{(1)}(\omega) & G_{14}^{(1)}(\omega) & G_{15}^{(1)}(\omega) & G_{16}^{(1)}(\omega) \\ G_{21}^{(1)}(\omega) & G_{22}^{(1)}(\omega) & G_{23}^{(1)}(\omega) & G_{24}^{(1)}(\omega) & G_{25}^{(1)}(\omega) & G_{26}^{(1)}(\omega) \\ G_{31}^{(1)}(\omega) & G_{32}^{(1)}(\omega) & G_{33}^{(1)}(\omega) & G_{34}^{(1)}(\omega) & G_{35}^{(1)}(\omega) & G_{36}^{(1)}(\omega) \\ \vdots & \vdots & \vdots & \vdots & \vdots & \vdots \\ G_{11}^{(N)}(\omega) & G_{12}^{(N)}(\omega) & G_{13}^{(N)}(\omega) & G_{14}^{(N)}(\omega) & G_{15}^{(N)}(\omega) & G_{16}^{(N)}(\omega) \\ G_{21}^{(N)}(\omega) & G_{22}^{(N)}(\omega) & G_{23}^{(N)}(\omega) & G_{24}^{(N)}(\omega) & G_{25}^{(N)}(\omega) & G_{26}^{(N)}(\omega) \\ G_{31}^{(N)}(\omega) & G_{32}^{(N)}(\omega) & G_{33}^{(N)}(\omega) & G_{34}^{(N)}(\omega) & G_{35}^{(N)}(\omega) & G_{36}^{(N)}(\omega) \end{bmatrix} \begin{bmatrix} m_{11}(w) \\ m_{22}(w) \\ m_{33}(w) \\ m_{44}(w) \\ m_{55}(w) \\ m_{66}(w) \end{bmatrix} \tag{12}$$

Or in a simple form of

$$d = Gm. \tag{13}$$

For each frequency ω, this equation is solved for $m = (m_{11}(w), m_{22}(w), m_{33}(w), m_{44}(w), m_{44}(w), m_{66}(w))$. Once, solved for all the frequencies, it will result into a $(n\omega \times 6)^{\ddagger}$ matrix of $m(\omega)$. Then taking Fourier transform of

$^{\ddagger}n\omega$ is the number of frequencies.

each column of this $m(\omega)$ matrix will result in the $m(t)$ matrix with the six time-dependent moment tensor vectors, $m(t) = (m_{11}(t), m_{22}(t), m_{33}(t), m_{23}(t), m_{13}(t), m_{12}(t))$. Vasco (1989) took the singular value decomposition of this $m(t)$ matrix, then showed that the eigenvector associated with the largest singular value is the source-time function (equation 2). At this point it is not clear to us why this decomposition will results in the source function and we shall put more thought into this in near future.

We applied this method on TIGER generated data from two receiver's array configuration and obtained a source-time function. Knowing the initial wavelet which we input to TIGER software, Figure 7 presented a comparisons of the initial wavelet and the estimated source-time function. There is a very good match between the estimated source-time function and the second derivative of the initial wavelet used in the modleing. Based on equations 4 and 5, we were expecting such a match for the first derivative of the initial wavelet. It is unclear to us, how actually TIGER software deals with the wavelet generation. This is a matter to be addressed in near future.

Step 2: Time-domain waveform inversion for moment tensor

Now that the source-time function is estimated, it will be taken out of the displacement wavefield. In this regard, the elementary seismograms and their spacial derivatives are defined as

$$E_{np}(\vec{x}, t) = S(t) * g_{np}(\vec{x}, t), \tag{14}$$

$$E_{np,q}(\vec{x}, t) = S(t) * g_{np,q}(\vec{x}, t). \tag{15}$$

Substituting the elementary functions into equation 1, the displacement components become

$$u_n(\vec{x}, t) = M_{pq} E_{np,q}(\vec{x}, t). \tag{16}$$

With the same fashion as we practised in defining the 18 G_{ij} functions (see Appendix B), these elementary functions can be treated to obtain 18 E_{ij} functions. An an example Figure 10 displays the E_{22} function. By constructing the E_{ij} functions, a linear system of equation can be set up to solve for M_{pq} as follows:

$$\begin{bmatrix} u_1^{(1)}(t_1) \\ u_2^{(1)}(t_1) \\ u_3^{(1)}(t_1) \\ \vdots \\ u_1^{(1)}(t_{nt}) \\ u_2^{(1)}(t_{nt}) \\ u_3^{(1)}(t_{nt}) \\ \vdots \\ u_1^{(N)}(t_1) \\ u_2^{(N)}(t_1) \\ u_3^{(N)}(t_1) \\ \vdots \\ u_1^{(N)}(t_{nt}) \\ u_2^{(N)}(t_{nt}) \\ u_3^{(N)}(t_{nt}) \end{bmatrix} = \begin{bmatrix} E_{11}^{(1)}(t_1) & E_{12}^{(1)}(t_1) & E_{13}^{(1)}(t_1) & E_{14}^{(1)}(t_1) & E_{15}^{(1)}(t_1) & E_{16}^{(1)}(t_1) \\ E_{21}^{(1)}(t_1) & E_{22}^{(1)}(t_1) & E_{23}^{(1)}(t_1) & E_{24}^{(1)}(t_1) & E_{25}^{(1)}(t_1) & E_{26}^{(1)}(t_1) \\ E_{31}^{(1)}(t_1) & E_{32}^{(1)}(t_1) & E_{33}^{(1)}(t_1) & E_{34}^{(1)}(t_1) & E_{35}^{(1)}(t_1) & E_{36}^{(1)}(t_1) \\ \vdots & \vdots & \vdots & \vdots & \vdots & \vdots \\ E_{11}^{(1)}(t_{nt}) & E_{12}^{(1)}(t_{nt}) & E_{13}^{(1)}(t_{nt}) & E_{14}^{(1)}(t_{nt}) & E_{15}^{(1)}(t_{nt}) & E_{16}^{(1)}(t_{nt}) \\ E_{21}^{(1)}(t_{nt}) & E_{22}^{(1)}(t_{nt}) & E_{23}^{(1)}(t_{nt}) & E_{24}^{(1)}(t_{nt}) & E_{25}^{(1)}(t_{nt}) & E_{26}^{(1)}(t_{nt}) \\ E_{31}^{(1)}(t_{nt}) & E_{32}^{(1)}(t_{nt}) & E_{33}^{(1)}(t_{nt}) & E_{34}^{(1)}(t_{nt}) & E_{35}^{(1)}(t_{nt}) & E_{36}^{(1)}(t_{nt}) \\ \vdots & \vdots & \vdots & \vdots & \vdots & \vdots \\ E_{11}^{(N)}(t_{nt}) & E_{12}^{(N)}(t_{nt}) & E_{13}^{(N)}(t_{nt}) & E_{14}^{(N)}(t_{nt}) & E_{15}^{(N)}(t_{nt}) & E_{16}^{(N)}(t_{nt}) \\ E_{21}^{(N)}(t_{nt}) & E_{22}^{(N)}(t_{nt}) & E_{23}^{(N)}(t_{nt}) & E_{24}^{(N)}(t_{nt}) & E_{25}^{(N)}(t_{nt}) & E_{26}^{(N)}(t_{nt}) \\ E_{31}^{(N)}(t_{nt}) & E_{32}^{(N)}(t_{nt}) & E_{33}^{(N)}(t_{nt}) & E_{34}^{(N)}(t_{nt}) & E_{35}^{(N)}(t_{nt}) & E_{36}^{(N)}(t_{nt}) \\ \vdots & \vdots & \vdots & \vdots & \vdots & \vdots \\ E_{11}^{(N)}(t_{nt}) & E_{12}^{(N)}(t_{nt}) & E_{13}^{(N)}(t_{nt}) & E_{14}^{(N)}(t_{nt}) & E_{15}^{(N)}(t_{nt}) & E_{16}^{(N)}(t_{nt}) \\ E_{21}^{(N)}(t_{nt}) & E_{22}^{(N)}(t_{nt}) & G_{23}^{(N)}(t_{nt}) & E_{24}^{(N)}(t_{nt}) & E_{25}^{(N)}(t_{nt}) & E_{26}^{(N)}(t_{nt}) \\ E_{31}^{(N)}(t_{nt}) & E_{32}^{(N)}(t_{nt}) & G_{33}^{(N)}(t_{nt}) & E_{34}^{(N)}(t_{nt}) & E_{35}^{(N)}(t_{nt}) & E_{36}^{(N)}(t_{nt}) \end{bmatrix}_{(3ntN\times 6)} \begin{bmatrix} M_{11} \\ M_{22} \\ M_{33} \\ M_{44} \\ M_{55} \\ M_{66} \end{bmatrix} \tag{17}$$

This time-domain linear inversion is done using a damped least-squares method. The interesting thing about it is that its a waveform inversion, with no need of picking P- and S-wave arrival amplitudes, and yet applied in a linear fashion.

We applied this time-domain waveform inversion on the TIGER data, inverting for the source moment tensor, and obtained promising results but not the exact moment tensor that we used in the modelling. Retrieving the exact M_{pq} is expected for such noise free data with accurate source location and velocity model, which requires more research at this point.

CONCLUSIONS AND FUTURE WORK

This research focused on retrieving an accurate seismic moment tensor from the amplitude inversion of 3C microseismic data. Our research consisted of two parts. Part 1, linear inversion of P- and S-wave first-arrival amplitudes in the time domain, and part 2 inversion of the seismic waveform in both the time and frequency domains.

In part 1, we used linear amplitude inversion of P- and S-wave first-arrival amplitudes, to investigate the optimal microseismic acquisition that resolves the full moment tensor. To remain consistent with previous research results on this topic by Vavryčuk (2007); Eaton and Forouhideh (2011); Rodriguez et al. (2011) we found that any two vertical or surface receiver arrays, or any combination of them, as long as they constitute different azimuths with respect to the source, are appropriate acquisition configurations. Importantly for a single well geometry, the most common practiced microseismic acquisition geometry, by having receiver arrays in both vertical and horizontal part of the deviated well, the seismic moment tensor is fully resolvable. In this investigation, we assumed accurate source location and velocity model, so as to investigate the effect of receiver geometry only.

In part 2, to avoid picking of P- and S-wave arrival amplitudes, we investigated a seismic waveform inversion proposed by Vavryčuk and Kühn (2012) with two steps. In step 1, we estimated the source-time function using a frequency domain inversion followed by the principal decomposition method (Vasco, 1989). In step 2, we formulated a linear waveform

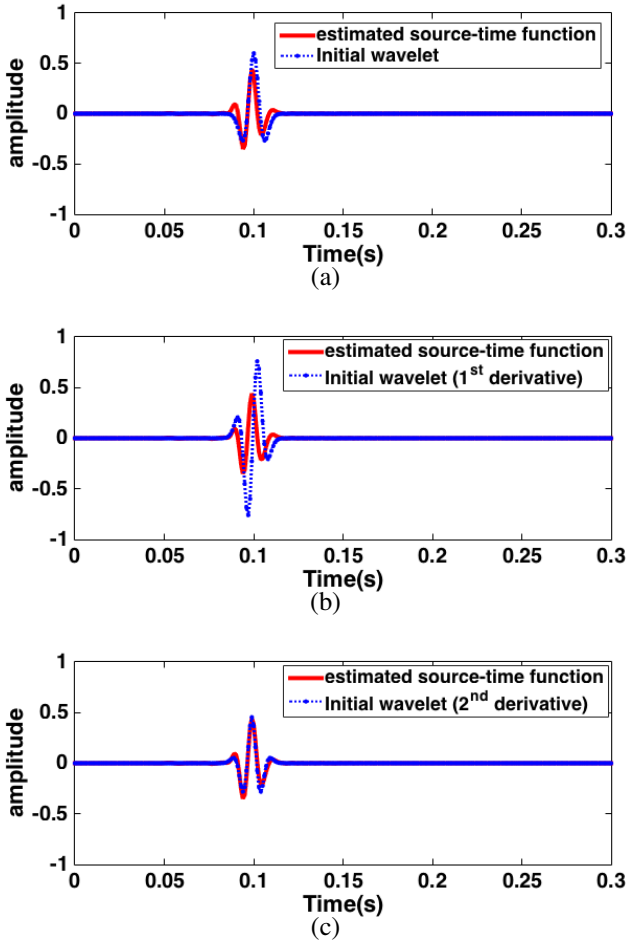

FIG. 7: Comparison of the estimated source-time function with (a) initial wavelet with the dominant frequency of 150HZ, (b) the first derivative of the initial wavelet. (c) the second derivatives of the initial wavelet.

inversion at all time samples, and used the source-time function calculated at step 1 in a linear waveform inversion for M_{pq} in the time domain. We were able to accurately estimate the source time function, but the accurate estimation of M_{pq} requires further research and will be addressed in near future. We shall also investigate the effect of errors in the source location and in the velocity model, including the possible effect of the anisotropy. Our ultimate goal is to apply a full seismic waveform inversion for the velocity model and moment tensor simultaneously.

ACKNOWLEDGMENTS

We thank NSERC (Natural Science and Engineering Research Council of Canada) and the sponsors of CREWES for their financial support. We thank SINTEFF for providing access to TIGER modelling software. We appreciate Dr. Gary Margrave for several discussions, Gary picked up a mistake early on, without his guidance this research wouldn't be possible. Dr. P.F. Daley is greatly appreciated for editing the manuscript for English grammar and style. Dr. Joe Wong is acknowledged for his suggestion to start the moment

tensor research with TIGER data rather than acquiring physical modelling data. Hormoz Izadi is acknowledged for his help in setting up Faranak with Latex editor on her new Mac computer. Ye Geng is acknowledged for her help in fixing Tiger data formatting.

APPENDIX A
Moment tensor decomposition

This appendix presents some terminology related to moment tensor decomposition, although the decomposition procedure is not presented in this report and shall be used for future research.

The pair of force couples (M_{pq}, M_{qp}) is termed a **double-couple** (DC) force (Figure 8(b)). The pure DC component is associated with shear faulting. For example, M_{12} is associated to the vertical fault as in Figure 9 (left), because $M_{12} = M_{21}$, is also the representative of the vertical fault as in Figure 9 (right). Then, its moment tensor becomes

$$M_{DC} = \begin{bmatrix} 0 & M_0 & 0 \\ M_0 & 0 & 0 \\ 0 & 0 & 0 \end{bmatrix}, \tag{18}$$

where M_0 is scalar seismic moment defining the associated earthquake magnitude. In general there are two fault planes that are consistent with distant seismic observation in the DC model (Shearer, 1999).

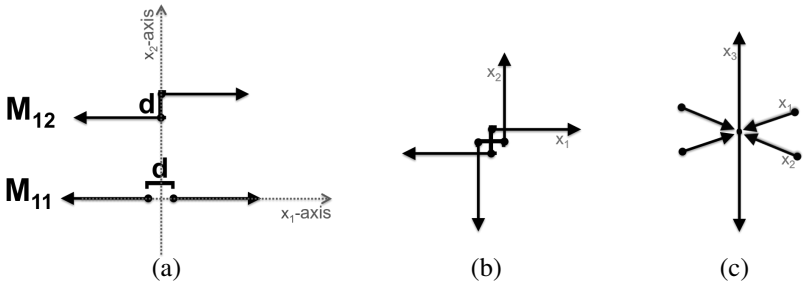

FIG. 8: (a) Force couples, M_{11} and M_{12}. (b) Double couple (M_{12} and M_{21}). (c) The CLVD of equation 21.

The moment tensor for an explosive source, is called **isotropic** and it has the simple form of

$$M_{ISO} = \begin{bmatrix} M_0 & 0 & 0 \\ 0 & M_0 & 0 \\ 0 & 0 & M_0 \end{bmatrix}. \tag{19}$$

A **linear dipole** source is represented by a moment tensor with a single non-zero diagonal element, for example

$$M_{LD} = \begin{bmatrix} M_0 & 0 & 0 \\ 0 & 0 & 0 \\ 0 & 0 & 0 \end{bmatrix}. \tag{20}$$

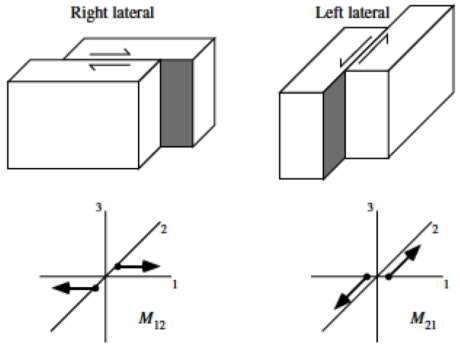

FIG. 9: These two faults have the same moment tensor representation and radiation pattern (Shearer, 1999).

The compensated linear vector dipole (CLVD) has a double-strength force couple along one axis, which are compensated by two unit strength force couples in the direction of two perpendicular directions (Lay and Wallace, 1995), for example (Figure 8c)

$$M_{CLVD} = \begin{bmatrix} -M_0 & 0 & 0 \\ 0 & -M_0 & 0 \\ 0 & 0 & 2M_0 \end{bmatrix}. \tag{21}$$

The symmetric moment tensor can be diagonalized by computing its eigenvalues and eigenvectors. For example, the representative moment tensor of shear faults in Figure 8 in the coordinate system aligned with its eigenvectors becomes

$$M_{DC} = \begin{bmatrix} M_0 & 0 & 0 \\ 0 & -M_0 & 0 \\ 0 & 0 & 0 \end{bmatrix}. \tag{22}$$

When a source moment tensor diagonalized, its trace is a measure of volume associated with that source. For example, the volume change that accompany the faults in Figure 8 is zero (equation 22), also true for any other shear faulting, DC source. In contrast, the volume change of an isotropic explosive source is positive (equation 19). A CLVD source produces no volume change (equation 21),.

Once a moment tensor diagonalize, it can be further restructured to form three basic types: the isotropic, double-couple, and CLVD (e.g., Dziewonski et al., 1981; Jost and Hermann, 1996; Vavryčuk, 2015)

$$M = M_{ISO} + M_{DC} + M_{CLVD}. \tag{23}$$

APPENDIX B
P- and S-wave radiation pattern and Green's function

In this appendix, we explain the simplified version of the radiation patterns and Green's function, for a homogenous isotropic medium, that is used in our MatLab codes for the

moment tensor inversion. Starting by P-wave, equation 4, we rewrite the *n*th component of the P-wave radiation pattern as

$$\mathscr{F}_n^P(\vec{x}) = A\gamma_n \left(\sum_p \gamma_p \sum_q M_{pq}\gamma_q \right), \tag{24}$$

where the indexes p and q are $(1, 2, 3)$, and $A = 1/4\pi\rho\alpha^3 r$ is written for simplicity. This has the form of matrix multiplication, hence the three-component P-wave radiation pattern can be written using matrix multiplication as follow

$$\begin{bmatrix} \mathscr{F}_1^P \\ \mathscr{F}_2^P \\ \mathscr{F}_3^P \end{bmatrix}_{3\times1} = A \begin{bmatrix} \gamma_1 \\ \gamma_2 \\ \gamma_3 \end{bmatrix}_{3\times1} \begin{bmatrix} \gamma_1 & \gamma_2 & \gamma_3 \end{bmatrix}_{1\times3} \begin{bmatrix} M_{11} & M_{12} & M_{13} \\ M_{21} & M_{22} & M_{23} \\ M_{31} & M_{32} & M_{33} \end{bmatrix}_{3\times3} \begin{bmatrix} \gamma_1 \\ \gamma_2 \\ \gamma_3 \end{bmatrix}_{3\times1}. \tag{25}$$

The radiation pattern (equation 24), or the displacement at first place (equation 4), is a linear function of M_{pq}. Hence expanding equation 25 further, the 3C of P-wave radiation pattern can be written as linear functions of the six independent M_{pq} as

$$\begin{bmatrix} \mathscr{F}_1^P \\ \mathscr{F}_2^P \\ \mathscr{F}_3^P \end{bmatrix} = A \begin{bmatrix} \gamma_1^3 & \gamma_1\gamma_2^2 & \gamma_1\gamma_3^3 & 2\gamma_1\gamma_2\gamma_3 & 2\gamma_1^2\gamma_3 & 2\gamma_1^2\gamma_2 \\ \gamma_2\gamma_1^2 & \gamma_2^3 & \gamma_2\gamma_3^2 & 2\gamma_2^2\gamma_3 & 2\gamma_2\gamma_1\gamma_3 & 2\gamma_2^2\gamma_1 \\ \gamma_3\gamma_1^2 & \gamma_3\gamma_2^2 & \gamma_3^3 & 2\gamma_3^2\gamma_2 & 2\gamma_3^2\gamma_1 & 2\gamma_3\gamma_1\gamma_2 \end{bmatrix}_{3\times6} \begin{bmatrix} M_{11} \\ M_{22} \\ M_{33} \\ M_{23} \\ M_{13} \\ M_{12} \end{bmatrix}_{6\times1}. \tag{26}$$

We used this linear expression to code up the P-wave radiation pattern. In a simple form, equation 26 can be equivalently written as:

$$\mathscr{F}^P = \underline{G}^P M. \tag{27}$$

As stated before, the Green's functions are just the radiation patterns without the source moment tensor term. To obtain the Green's functions, following Vavryčuk and Kühn (2012), we reduce the pair of indices in $g_{np,q}$ (equation 6) and define the $G_{kj}(k = 1 : 3 \text{ and } j = 1 : 6)$ functions as

$$\begin{aligned} &G_{k1} = g_{k1,1}, && G_{k2} = g_{k2,2}, && G_{k3} = g_{k3,3}, \\ &G_{k4} = g_{k2,3} + g_{k3,2}, && G_{k5} = g_{k1,3} + g_{k3,1}, && G_{k6} = g_{k1,2} + g_{k2,1}. \end{aligned} \tag{28}$$

There are 18 of such defined P-wave (G_{kj}) functions. T hey are in fact reduced forms of the special derivatives of the Green's functions with only two indexes. Then, it can be easily shown that the values of newly defined G_{ij} functions, at P-wave arrival time, are element of matrix $\underline{G}^P$ in equation 27:

$$\begin{bmatrix} G11 & G12 & G13 & G14 & G15 & G16 \\ G21 & G22 & G23 & G24 & G25 & G26 \\ G31 & G32 & G33 & G34 & G35 & G36 \end{bmatrix} = A \begin{bmatrix} \gamma_1^3 & \gamma_1\gamma_2^2 & \gamma_1\gamma_3^3 & 2\gamma_1\gamma_2\gamma_3 & 2\gamma_1^2\gamma_3 & 2\gamma_1^2\gamma_2 \\ \gamma_2\gamma_1^2 & \gamma_2^3 & \gamma_2\gamma_3^2 & 2\gamma_2^2\gamma_3 & 2\gamma_2\gamma_1\gamma_3 & 2\gamma_2^2\gamma_1 \\ \gamma_3\gamma_1^2 & \gamma_3\gamma_2^2 & \gamma_3^3 & 2\gamma_3^2\gamma_2 & 2\gamma_3^2\gamma_1 & 2\gamma_3\gamma_1\gamma_2 \end{bmatrix}. \tag{29}$$

Similarly for the S-wave radiation pattern, we rewrite the S-wave radiation pattern (equation 5) as

$$\mathscr{F}_n^S(\vec{x}) = B \left(\sum_p \delta_{np} \sum_q M_{pq}\gamma_q - \gamma_n \sum_p \gamma_p \sum_q M_{pq}\gamma_q \right), \tag{30}$$

where $B = 1/4\pi\rho\beta^3 r$ is written for simplicity. Then using the matrix multiplication, the S-wave radiation pattern reads into

$$\frac{1}{B}\begin{bmatrix}\mathscr{F}_1^S\\ \mathscr{F}_2^S\\ \mathscr{F}_3^S\end{bmatrix} = \begin{bmatrix}1&0&0\\0&1&0\\0&0&1\end{bmatrix}_{3\times3}\begin{bmatrix}M_{11}&M_{12}&M_{13}\\M_{21}&M_{22}&M_{23}\\M_{31}&M_{32}&M_{33}\end{bmatrix}_{3\times3}\begin{bmatrix}\gamma_1\\\gamma_2\\\gamma_3\end{bmatrix}_{3\times1} - \begin{bmatrix}\gamma_1\\\gamma_2\\\gamma_3\end{bmatrix}_{3\times1}\begin{bmatrix}\gamma_1&\gamma_2&\gamma_3\end{bmatrix}_{1\times3}\begin{bmatrix}M_{11}&M_{12}&M_{13}\\M_{21}&M_{22}&M_{23}\\M_{31}&M_{32}&M_{33}\end{bmatrix}_{3\times3}\begin{bmatrix}\gamma_1\\\gamma_2\\\gamma_3\end{bmatrix}_{3\times1}. \tag{31}$$

Further it can equivalently be written as:

$$\frac{1}{B}\begin{bmatrix}\mathscr{F}_1^S\\ \mathscr{F}_2^S\\ \mathscr{F}_3^S\end{bmatrix} = \begin{bmatrix}\gamma_1-\gamma_1^3 & -\gamma_1\gamma_2^2 & -\gamma_1\gamma_3^2 & -2\gamma_1\gamma_2\gamma_3 & \gamma_3-2\gamma_1^2\gamma_3 & \gamma_2-2\gamma_1^2\gamma_2\\ -\gamma_2\gamma_1^2 & \gamma_2-\gamma_2^3 & -\gamma_2\gamma_3^2 & \gamma_3-2\gamma_2^2\gamma_3 & -2\gamma_2\gamma_1\gamma_3 & \gamma_1-2\gamma_2^2\gamma_1\\ -\gamma_3\gamma_1^2 & -\gamma_3\gamma_2^2 & \gamma_3-\gamma_3^3 & \gamma_2-2\gamma_3^2\gamma_2 & \gamma_1-2\gamma_3^2\gamma_1 & -2\gamma_3\gamma_1\gamma_2\end{bmatrix}_{3\times6}\begin{bmatrix}M_{11}\\M_{22}\\M_{33}\\M_{23}\\M_{13}\\M_{12}\end{bmatrix}_{6\times1}. \tag{32}$$

We used this linear expression to code up the S-wave radiation patterns. The values of $G_{kj}(\vec{x},t)$ functions at S-wave arrival times will similarly be as following:

$$\begin{bmatrix}G11&G12&G13&G14&G15&G16\\G21&G22&G23&G24&G25&G26\\G31&G32&G33&G34&G35&G36\end{bmatrix} = B\begin{bmatrix}\gamma_1-\gamma_1^3 & -\gamma_1\gamma_2^2 & -\gamma_1\gamma_3^2 & -2\gamma_1\gamma_2\gamma_3 & \gamma_3-2\gamma_1^2\gamma_3 & \gamma_2-2\gamma_1^2\gamma_2\\ -\gamma_2\gamma_1^2 & \gamma_2-\gamma_2^3 & -\gamma_2\gamma_3^2 & \gamma_3-2\gamma_2^2\gamma_3 & -2\gamma_2\gamma_1\gamma_3 & \gamma_1-2\gamma_2^2\gamma_1\\ -\gamma_3\gamma_1^2 & -\gamma_3\gamma_2^2 & \gamma_3-\gamma_3^3 & \gamma_2-2\gamma_3^2\gamma_2 & \gamma_1-2\gamma_3^2\gamma_1 & -2\gamma_3\gamma_1\gamma_2\end{bmatrix}. \tag{33}$$

For a homogeneous isotropic medium, the above 18 G_{kj} functions could be considered as time series with their defined values at P-wave arrival time ($t_p = r/\alpha$) and S-wave arrival time ($t_s = r/\beta$). As an example the time-dependent $G_{22}(\vec{x},t)$ function is shown in Figure 10(a).

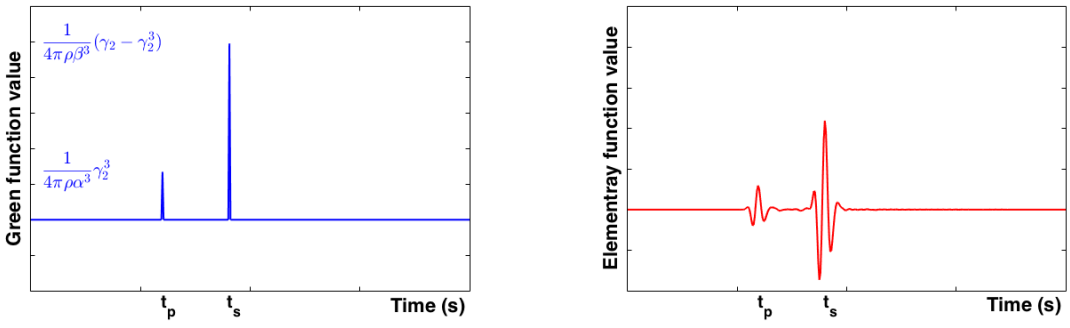

(a) (b)

FIG. 10: (a) The function $G_{22}(\vec{x},t)$ for a receiver point at $\vec{x}$, where $\gamma_i = \frac{(\vec{x}-\vec{x_s})_i}{r}$ and r is source-receiver distance as defined before. Note, the G_{22} contains the elements indexed $(2,2)$ of the Green function matrix in equations 29 and 33. (b) The elementary function E_{22}, the convolution of the G_{22} function and the source-time function.

APPENDIX C
Generating synthetics microseismic data using TIGER

This appendix presents some details on how to generate synthetics microseismic data using TIGER, a 3D anisotropic elastic finite-difference modelling software from SINTEF Petroleum Research. The finite-difference code is capable of generating accurate seismic datasets with minimal dispersion. TIGER is able to generate 3C data for 3D anisotropic models. The code is developed to simulate seismic modelling for transverse-isotropy media with tilted symmetry axis. However we only run it for a homogeneous isotropic medium for the purpose of this report. The wave propagation can be initiated by a general source moment tensor in TIGER. Also, the software has been implemented for general source and receiver geometries. Hence, TIGER is capable of modelling microseismic activities. Here we examine the accuracy of TIGER produced data when the wave propagation is initiated by a source moment tensor.

To produce microseismic synthetics data, we used several borehole and receiver arrays. Figure 11 displays the TIGER interface when generating data recorded at a single vertical receiver array, for a buried point source with the moment tensor M as in equation 10. The interface contains displays of the velocity/density model, the source-time function, and source and receiver locations.

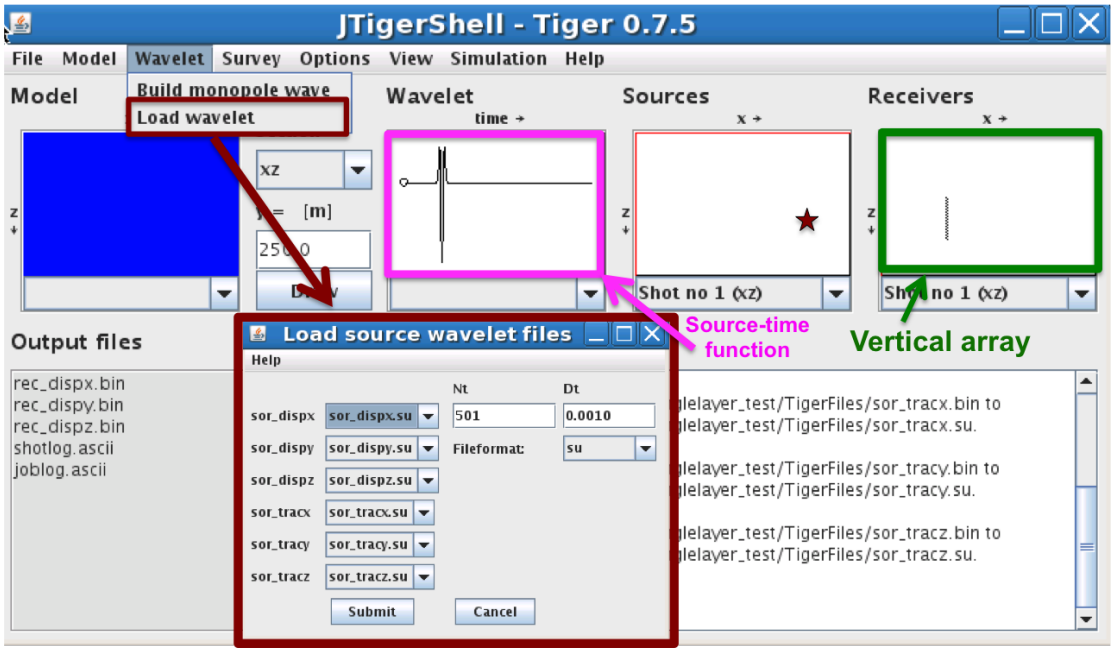

FIG. 11: The six moment tensor wavelets (shown in the red box) input in TIGER; from top to bottom they are associated with $M_{11}, M_{22}, M_{33}, M_{23}, M_{13}, M_{12}$ respectively. The source-time function (shown in pink box) has the dominate frequency of 150HZ. The source is buried at a depth, and the vertical array receiver's are shown in the green box.

TIGER accepts six different input wavelets which each directly represents the components of M matrix. We used a Ricker wavelet with a dominate frequency of 150 HZ as the source-time function, to mimic the high frequency content of microseismic data. This source-time function is then scaled using each M_{pq} value to create the required six mo-

ment tensor wavelets. Generating the wavelets is done outside the TIGER and then the six wavelets are input in the "Load wavelet" tab in TIGER interface (Figure 11) .

Next we examined the accuracy of TIGER produced synthetics data. The expected theoretical values are calculated using 3C P- and S-wave displacement values using equations 4 and 5. It is expected that TIGER data have the same radiation pattern as this theoretical values. Also, we convolve the source-time function with the calculated Green's function and generated the expected 3C synthetics (called **modelled data 1**) and compared it to TIGER generated synthetics; see Appendix D on how to calculate the Green's functions for a homogenous isotropic medium. For a vertical receiver array located at azimuth $45°$[§] to the source (with respect to the reference coordinate system), we generated the 3C TIGER data. The source is located at $(400m, 400m, 300m)$, the shallowest receiver is located at $(150m, 150m, 225m)$, the receiver interval is 10m, and the borehole receiver array contains the total of 15 receivers (the lowest receiver is located at $(150m, 150m, 365m)$. Figure 12 shows the 3C TIGER synthetics in red blue, and the **modelled data 1** in red color. There is very good agreement between the **modelled data 1** and the TIGER data conforming the accuracy of the TIGER data for a general moment tensor source. Figure refdisplacement shows the theoretical 3D displacement P- and S-wave amplitudes generated using equations 4 and 5.

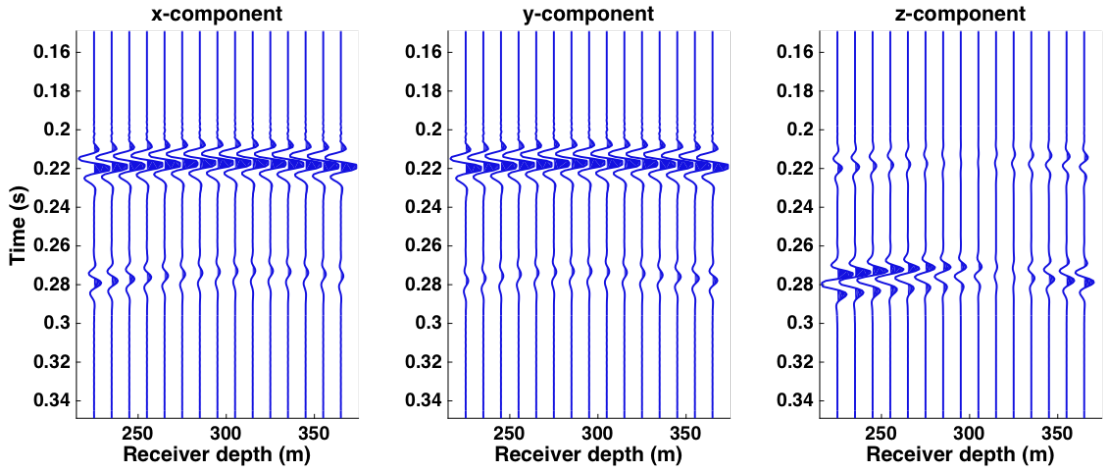

FIG. 12: 3C synthetics data generated by TIGER using the seismic moment tensor as in equation 10. Note each panel has been scaled differently.

REFERENCES

Aki, K., and Richards, P. G., 2002, Quantitative Seismology: W. H. Freeman and Company, San Francisco.

Dziewonski, A., Chou, T., and Woodhouse, J., 1981, Determination of earthquake source parameters from waveform data for studies of global and regional seismicity: J. Geophys. Res., **86**, No. B4, 2825–2852.

Eaton, D. W., and Forouhideh, F., 2011, The role of passive microseismic monitoring in the instrumented oil field: The Leading Edge, **76**, No. 6, WC77–WC85.

Ebel, J. E., and Bonjer, K. P., 1990, Moment tensor inversion of small earthquakes in southwestern germany for the fault plane solution: Geophys. J. Int., **101**, No. 6, 133–146.

[§]Note, this receiver array is different from the vertical array shown in the Figure 11.

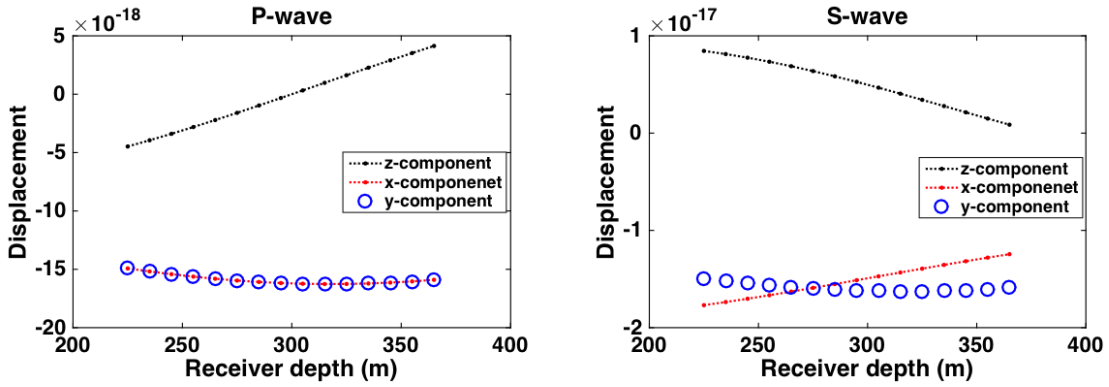

FIG. 13: Expexted 3C displacement amplitudes calculated using equations 4 and 5 .

Eyre, T. S., and van der Baan, M., 2015, Overview of moment-tensor inversion of microseismic events: The Leading Edge, **34**, No. 8, 882–888.

Foulger, G. R., Julian, B. R., Hill, D. P., Pitt, A. M., and Malin, P. E., 2004, Non-double-couple microearthquakes at long valley caldera, california, provide evidence for hydraulic fracturing: Journal of Volcanology and Geothermal Research, **132**, 45–71.

Hardebeck, J. L., and Shearer, P. M., 2003, Using s/p amplitude ratio to constrain the focal mechanisms of small earthquakes: Bull. Seism. Soc. Am., **93**, No. 6, 12,434–12,444.

Jost, M. L., and Hermann, R. B., 1996, A student's guide to and review of moment tensors: Seismological Research Letters, **60**, No. 2, 37–57.

Julian, B. R., and Foulger, G. R., 1996, Earthquake mechanisms from linear-programming inversion of seismic-wave amplitude ratios: Bull. Seism. Soc. Am., **86**, 974–980.

Lay, T., and Wallace, T. C., 1995, Modern Global Seismology: Academic Press.

Madariaga, R., 2007, Seismic Source Theory, in H. Kanamori, ed., Earthquake Seismology: Elsevier.

Mahmoudian, F., Margrave, G. F., Wong, J., and Henley, D., 2015, Azimuthal amplitude variation with offset analysis of physical modeling data acquired over an azimuthally anisotropic medium: Geophysics, **80**.

Maxwell, S. C., and Urbancic, T. I., 2001, The role of passive microseismic monitoring in the instrumented oil field: The Leading Edge, **20**, 636–640.

Menke, W., 1985, Geophysical Data Analysis: Discrete Inversion Theory: Academic Press.

Nakamura, A., Horiuchi, S., and Hasegawa, A., 1999, Joint focal mechanism determination with source-region station corrections using shortperiod body-wave amplitude data: Bull. Seism. Soc. Am., **89**, No. 6, 373Ð383.

Nolen-Hoeksema, R. C., and Ruff, L. J., 2001, Moment tensor inversion of microseisms from the b-sand propped hydrofracture, m-site, colorado: Tectonophysics, **336**, 163–181.

Rau, R. J., Wu, F. T., and Shin, T. C., 1996, Regional network focal mechanismdetermination using 3d velocity model and sh/p amplitude ratio: Bull. Seism. Soc. Am., **86**, 1270Ð1283.

Rodriguez, I. V., Gu, Y. J., and Sacchi, M. D., 2011, Resolution of seismic moment tensor inversions from a single array of receivers: Bulletin of the Seismological Society of America, **101**, No. 6.

Ross, A., Foulger, G. R., and Julian, B. R., 1999, Source processes of ndustrially-induced earthquakes at the geysers geothermal area, california: Geophysics, **64**, 1877–1889.

Shearer, P. M., 1999, Introduction to Seismology: Cambridge U Press.

Šílený, J., 1998, Earthquake source parameters and their confidence regions by a genetic algorithm with a 'memory': Geophys J. Int., **134**, 228–242.

Vasco, D. W., 1989, Deriving source-time functions using principal component analysis: Bull. Seism. Soc. Am., **79**, No. 3, 711–730.

Vavryčuk, V., 2001, Inversion fo rparameters of tensile earthquakes: Journal of Geophysical Research, **106**, No. B8, 16,339–16,355.

Vavryčuk, V., 2007, On the retrieval of moment tenors from borehole data: Geophysical Prospecting, **53**, 381–391.

Vavryčuk, V., 2015, Inversion for the Composite Moment Tensor: Bulletin of the Seismological Society of America, **105**, No. 6, 3024–3035.

Vavryčuk, V., and Kühn, D., 2012, Moment tensor inversion of waveforms: a two-step time-frequency approach: Geophysical Journal International, **190**, 1761–1776.